

# Adaptive NFC WPT System Implementing Neural Network-Based Impedance Matching with Bypass Functionality

J. Romero Lopera<sup>\*#</sup>, R. Fischbacher<sup>\*#</sup>, R. Pestros<sup>\*</sup>, D. Pommerenke<sup>\*\*</sup>, B. Auinger<sup>\*</sup>, J. Grosinger<sup>#</sup>

<sup>\*</sup>Silicon Austria Labs, TU-Graz SAL GEMC Lab, Austria

<sup>#</sup>Graz University of Technology, Austria

romerolopera@tugraz.at

**Abstract**—The work presents an adaptive impedance matching system controlled by an artificial neural network (ANN) for wireless power transfer (WPT) based on near-field communication (NFC) technology operating at 13.56 MHz. The system consists of two magnetically coupled resonators (MCRs) to establish wireless power transfer between a transmitter (TX) and receiver (RX). The MCR coils are based on class 1 standard NFC coils. In the TX, an adaptive impedance matching network (AIMN) is controlled by an ANN to optimize power transfer for changing TX-RX positions. Simulation and measurement data for changing TX-RX positions were used to train, validate, and test the ANN. A first analysis shows an improvement in the system's power transfer efficiency for varying positions. However, the matching gain is not always overcoming the losses introduced by the AIMN, which then leads to bypassing the matching network. In contrast to previous work, this work analyses NFC-based WPT systems based on class 1 coils for the first time, giving valuable insight for future real-time adaptive NFC WPT systems.

## I. INTRODUCTION

Wireless power transfer (WPT) systems based on magnetically coupled resonators (MCR) [1] are extensively used in wireless charging applications [2], and has been recently exploited as an additional functionality on commercial near field communications (NFC) systems [3]. WPT systems experience impedance variations at the input of the WPT transmitter MCR with a change of transmitter (TX) and receiver (RX) positions and, thus, an unfavorable performance degradation [4]. Several solutions have been proposed in the literature to overcome this issue, such as frequency tracking [5], coil repositioning [6], and adaptive impedance matching [7], [8]. Only the latter can keep the system optimized at the operating frequency for each TX-RX position [5], [9]. Some previous works use an artificial neural network (ANN) to adjust the adaptive matching network based on the TX-RX position [7], [8]. In this work, we present the concept of a real-time adaptive WPT system consisting of two MCRs in a series-series (SS) configuration [10], an adaptive impedance matching network (AIMN), and a control loop based on impedance detection and real-time actuation using an artificial neural network (ANN). The structure of the proposed system is shown in Figure 1. To analyze the realistic performance of NFC-based WPT systems, we use, in contrast to previous work, printed ISO/ICE 14443 class 1 coils in the MCRs, operating at 13.56 MHz. The presented system performance analysis shows that the losses introduced by the AIMN can overcome the matching gain in some situations, to bypass the network. Thus, we present for the first time

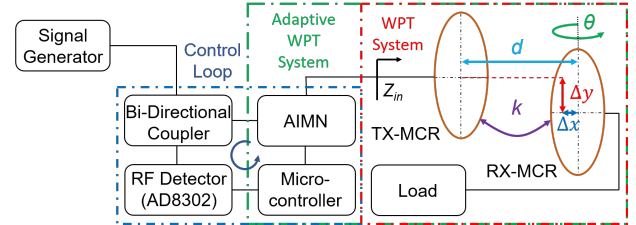


Fig. 1. Structure of the proposed real-time adaptive WPT system.

an AIMN bypass functionality. In addition, we provide a scattering parameter measurement dataset with our publication characterizing the WPT system for different TX-RX MCRs positions. The dataset can be used by other researchers to train an ANN or investigate NFC systems in general. The measured data is available under the following IEEE DataPort DOI: 10.21227/vtp8-x586.

## II. ADAPTIVE WPT SYSTEM

The proposed system in Fig. 1 consists of TX and RX MCRs. The RX MCR is connected to a load; the TX MCR is connected to an adaptive matching system to control the AIMN and keep the system matched at every TX-RX position using an ANN. The impedance detection hardware consists of a bi-directional coupler, a radio frequency (RF) detector, and a microcontroller. The input impedance  $Z_{in}$  at the input of the TX MCR is monitored by the adaptive matching system to optimize the system's power transfer efficiency (PTE) [7], [8].

### A. Magnetically Coupled Resonators

The MCRs consist of printed ISO/ICE 14443 class 1 coils and series capacitors [10], resonating at  $f_0 = 13.56$  MHz. The planar coils are printed on an FR4 substrate; their geometry is shown in Fig. 2. The coils were series resonated at  $f_0 = 13.56$  MHz using a capacitance of  $C_{res}$ . To determine the required capacitance  $C_{res}$ , the scattering parameters of the planar coils were measured using a R&S<sup>®</sup> ZNA 43 with the 50  $\Omega$  port 1 connected to the coil through a balun PWB3010L from Coilcraft for differential excitation at  $P_{in} = 0$  dBm. An equivalent circuit (EC) approximation for the coil at  $f_0$  was then considered [11] as shown in Fig. 3. For this work, 50  $\Omega$  load  $Z_L$  and source  $Z_S$  impedances are considered. The equivalent RF resistance  $R_{rf}$ , inductance  $L$ , and parallel capacitance  $C_p$  were determined based on the real and imaginary value of  $Z_{11}$  and the parallel self-resonance frequency [12]. The coupling coefficient  $k$  characterizes

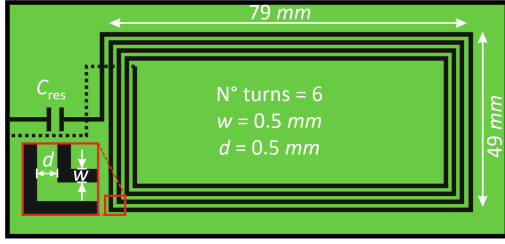


Fig. 2. Geometry of class 1 coils.

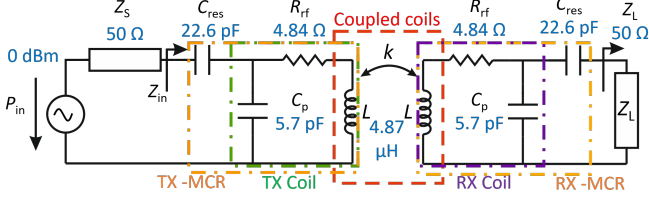


Fig. 3. EC representation of the WPT system: The RX is connected to a load  $Z_L$ . The transmitter coil is connected to an RF power source with impedance  $Z_S$  and power  $P_{in}$ .

the mutual coupling between the TX-RX coils. The tuning capacitance value was tuned to  $C_{res} = 22.4$  pF to resonate at  $f_0 = 13.56$  MHz. Fig. 3 shows all EC parameters.

### B. WPT System Measurements

We characterized the prototyped WPT system for different TX-RX positions. The two-port scattering parameters were measured under a parametric variation of misalignment in the x  $\Delta x$  and y  $\Delta y$  axis between the MCRs, azimuthal tilt  $\Theta$ , and distance  $d$ , as shown in Fig. 4 [13]. We used the same R&S<sup>®</sup>ZNA 43, baluns,  $Z_L$ ,  $Z_S$  and  $P_{in}$  as for the single coil scattering parameter measurements. We used a custom-built semi-automatized measurement setup to vary the RX MCR, allowing a manual fixing at different positions for  $\Delta x$  (0-60 mm, 10 mm steps),  $\Delta y$  (0-30 mm, 5 mm steps), and  $\Theta$  (0-60°, 15° steps). The measurement setup did an automatized scattering parameter measurement for different distances  $d$  (14-70 mm, 1 mm steps). In the cases of  $\Theta = 30^\circ, 45^\circ, 60^\circ$ , the closest distance  $d$  had to be increased to avoid physical collision of the coils, starting at  $d = [26, 38, 40]$  mm respectively. Additionally, an extended measurement range with a finer resolution was considered at the special cases  $\Delta x|_{\Delta y=0, \Theta=0^\circ}$  (0-60 mm, 5 mm steps),  $\Delta y|_{\Delta x=0, \Theta=0^\circ}$  (0-40 mm, 5 mm steps), and  $\Theta|_{\Delta x=0, \Delta y=0}$  (0-60°, 5° steps) to provide a finer characterization of each parameter independently. Altogether, the dataset provides 11,205 TX-RX configurations. Fig. 5 shows the WPT system measurement results in contour plots of the real and imaginary part of  $Z_{in}$  versus  $\Delta x$  and  $\Delta y$  for the configurations  $d = 14$  mm,  $\Theta = 0^\circ$  (1), and  $d = 36$  mm,  $\Theta = 60^\circ$  (2). The red contour lines indicate the points at which  $\text{Re}(Z_{in}) = 50 \Omega$  and  $\text{Im}(Z_{in}) = 0 \Omega$ , representing the critical coupling regions and the threshold between over- and under-coupled operation [6]. As expected, the real part decreases, and the imaginary part increases with increasing  $\Delta x$  and  $\Delta y$  due to decreased mutual coupling. In case 1, coupling between the

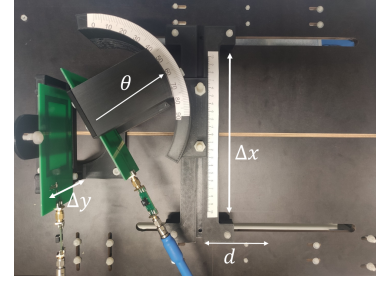


Fig. 4. Measurement setup for WPT system characterization.

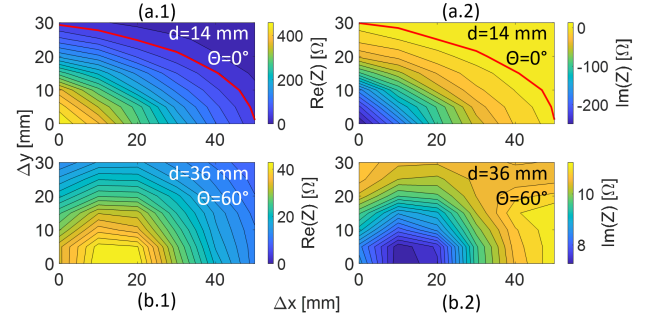


Fig. 5. Contour plots of TX MCR input impedance  $Z_{in}$  versus  $\Delta x$  and  $\Delta y$ .

MCRs is strong, requiring significant  $\Delta x, \Delta y$  misalignment until critical coupling occurs. In contrast, the larger  $d$  and  $\Theta$  values of case 2 cause coupling to be much lower. Under these conditions, the system is under-coupled for every  $\Delta x$  and  $\Delta y$ ; therefore, the critical coupling region is not present in the figure. The complete measured data is available under the following IEEE DataPort DOI: 10.21227/vtp8-x586.

### C. Adaptive Impedance Matching Network

An adaptive matching network based on [7] was designed to match the impedance  $Z_{in}$  to the source impedance  $Z_S$  and maximize WPT. The AIMN structure is shown in Fig. 6. The AIMN consists of cascaded L-type lowpass networks. Ceramic chip inductors of the Coilcraft 0603HL series were selected; their values are denoted in Fig. 6. These inductors have a moderate quality factor of 12-18 at 25 MHz; however, they were the only components providing the needed values for matching. As tuning elements, three LXRW19V201-058 voltage-controlled variable ceramic capacitors from Murata were allocated in shunt configuration as  $C_1$ ,  $C_2$  and  $C_3$  in the network. Their supply DC voltage ranges from 0-5 V. The impedance region that the AIMN network can match with a reflection coefficient better than  $-10$  dB is indicated in the  $50 \Omega$  normalized Smith chart in Fig. 6. Additionally, two RF switches, JSW2-63DR+ from Mini-circuits with 0.3 dB insertion loss, were implemented at the input and output of the AIMN to provide a bypass functionality. This bypass allows the accurate measurement of the impedance  $Z_{in}$  of the TX MCR by de-embedding the bypass. Furthermore, if the AIMN losses overcome the matching gain, as shown later in Fig. 7, the WPT efficiency of the system will be degraded, although the matching will be enhanced. The bypass then allows for overcoming this deteriorating effect of the matching network.

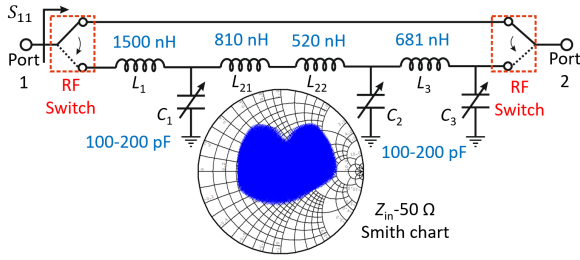


Fig. 6. Structure of the proposed AIMN and matched impedance region at 13.56 MHz with a reflection coefficient magnitude  $|S_{11}| < -10$  dB.

#### D. Artificial Neural Network

The AIMN will be driven by a microcontroller shown in Fig. 1 implementing an ANN with backpropagation [7], [8] using Matlab. Based on the TX MCR input impedance, the ANN decides how to adjust the tunable capacitor values of the AIMN to minimize the reflection coefficient  $S_{11}$  and maximize the transmission coefficient  $S_{21}$  of the AIMN (see Fig. 6). To train and validate the ANN [7], [8], we used Cadence's AWR to find the corresponding capacitor values  $C_1$ ,  $C_2$ , and  $C_3$  related to a general input impedance dataset with 8200 data points, i.e.,  $\text{Re}(Z_{\text{in}}) = (5-900) \Omega$  and  $\text{Im}(Z_{\text{in}}) = (-100-100) \Omega$  with a minimum of  $5 \Omega$  steps. 70 % of the labeled general dataset was used for training the ANN, whereas 30% of was used for validation. In addition, to test the ANN [7], [8], the corresponding capacitor values were related to the measured scattering parameters' dataset of the MCRs versus different positions (see, e.g., Fig.5). Using uncorrelated datasets is important to train, validate, and test the ANN [8]. For training, validating, and testing, the accuracy of the network is evaluated in terms of the mean squared error (MSE) of the capacitor values returned by the ANN ( $C_{\text{ANN}}$ ) and the optimized values from AWR ( $C_{\text{AWR}}$ ). The ANN's hyperparameters were adjusted during ANN validation by an iterative process, leading to 5 hidden layers and 15 neurons per layer [7], [8]. The MSE for ANN training and validation was 0.051 and 0.048, respectively ( $\approx 5\%$  variation or 5 pF).

### III. SYSTEM PERFORMANCE

To analyze the WPT system performance and test the ANN, the ANN has been implemented through Matlab into a custom-built virtual adaptive WPT system environment in AWR (see Fig. 1). The virtual WPT system includes the planar AIMN layout that is electromagnetic simulated, the commercial scattering parameter data of the lumped elements used in the AIMN, and the measured scattering parameter data of the TX-RX WPT system. Matlab acts as the microcontroller, steering the virtual adaptive WPT system environment in AWR. Input data from the measured dataset is sent to the ANN to predict the optimum capacitances required at the AIMN for each position. To analyze the WPT system performance, three representative coil positions versus distance  $d$  are investigated in more detail: state 1 ( $\Delta x = 0$  mm,  $\Delta y = 0$  mm,  $\Theta = 0^\circ$ ); state 2 ( $\Delta x = 20$  mm,  $\Delta y = 20$  mm,  $\Theta = 0^\circ$ ) and state 3 ( $\Delta x = 30$  mm,  $\Delta y = 25$  mm,  $\Theta = 0^\circ$ ). These positions represent different states of MCRs coupling, i.e., states with

decreasing coupling  $k$  ( $k_1 > k_2 > k_3$ ) for a given distance. Fig. 7 shows the results. The system performance is evaluated in terms of the reflection and transmission coefficients  $S_{11}$  and  $S_{21}$  versus  $d$  for an input power level of 0 dBm. Fig. 7a shows the measured real and imaginary parts of  $Z_{\text{in}}$ , as shown in Fig. 1 for the three states, following the theory [14], [9], [15]. At critical coupling, the impedances reach  $\text{Re}(Z_{\text{in}}) = Z_L = 50 \Omega$  and  $\text{Im}(Z_{\text{in}}) \approx 0 \Omega$  (see continuous grey arrows for states 1 and 2 in Fig. 7a). The fact that  $\text{Re}(Z_{\text{in}})$  decreases with decreasing  $k$  is another indicator that the SS-MCR works as intended. Fig. 7b depicts the magnitude of the reflection coefficient  $|S_{11}|$  dB, whereas Fig. 7c depicts the magnitude of the transmission coefficient  $|S_{21}|$  dB. The blue curves in Fig. 7b and 7c show the system using the AIMN and trained ANN for the three states. The red curves depict the WPT performance without the AIMN, i.e., bypassing the network.

The blue curves in Fig. 7b show that if the AIMN is active, the adaptive WPT system at all three states shows a significant enhancement in the matching for each distance, i.e.,  $|S_{11}| < -13$  dB. These results indicate an excellent prediction of the ANN, returning an MSE of 0.095 ( $\approx 10\%$  variation or 10 pF). ANN testing showed a lower accuracy than the ANN training and validation as expected [8]. The red curves in Fig. 7b show that if the AIMN is bypassed, a perfect match happens at critical coupling as expected from theory [14], [9], [15], i.e.,  $|S_{11}| = -20$  dB at distances  $d_{\text{state 1}} = 42$  mm and  $d_{\text{state 2}} = 27$  mm for states 1 and 2 respectively. State 3 does not show a local minimum at the investigated distances, indicating that the WPT system is operating in the under-coupling regime. The regions corresponding to over-/critical-/under-coupled operation at state 1 are indicated by the grey traces.

The blue curves in Fig. 7c show that if the AIMN is active,  $|S_{21}|$  dB stays at a constant value for a wide range of distances in each state, i.e.,  $|S_{21}| \approx -3$  dB. For distances far from the critical coupling point, the system is strongly over-/under-coupled, and  $|S_{21}|$  dB suffers degradation, reaching a minimum of  $|S_{21}| = -5$  dB for state 1 at  $d = 14$  mm and  $|S_{21}| = -4$  dB for state 3 at  $d = 70$  mm. For state 2,  $|S_{21}|$  dB presents a stable value  $-3.5 \text{ dB} < |S_{21}| < -3$  dB over distance  $d$ . In contrast, the red curves in Fig. 7b show that if the AIMN is bypassed, states 1 and 2 show a local maximum of  $|S_{21}| = -1.5$  dB at the point of critical coupling as expected from theory [14], [9], [15], whereas state 3 does not show a local maximum due to under-coupling operation for each distance  $d$ . The continuous grey arrows in Fig. 7c indicate the insertion loss (IL) in dB correspondent to the TX-RX MCRs (0.85 dB), RF switches (0.65 dB), and AIMN (1.52 dB) at critical coupling for states 1 and 2.  $\text{IL}_{\text{TX-RX MCR}}$  was extracted from the measured data of the WPT system,  $\text{IL}_{\text{RF switches}}$  was deducted from  $|S_{21}|$  dB of the bypassed AIMN without considering  $\text{IL}_{\text{TX-RX MCR}}$ . Finally,  $\text{IL}_{\text{AIMN}}$  was determined by the difference of the transmission coefficient magnitudes  $|S_{21}|$  dB between the red and blue curves at the critical coupling, representing an indicative value for the AIMN losses due to the insignificant mismatch loss.

The advantage of the AIMN improving  $|S_{11}|$  dB is visible



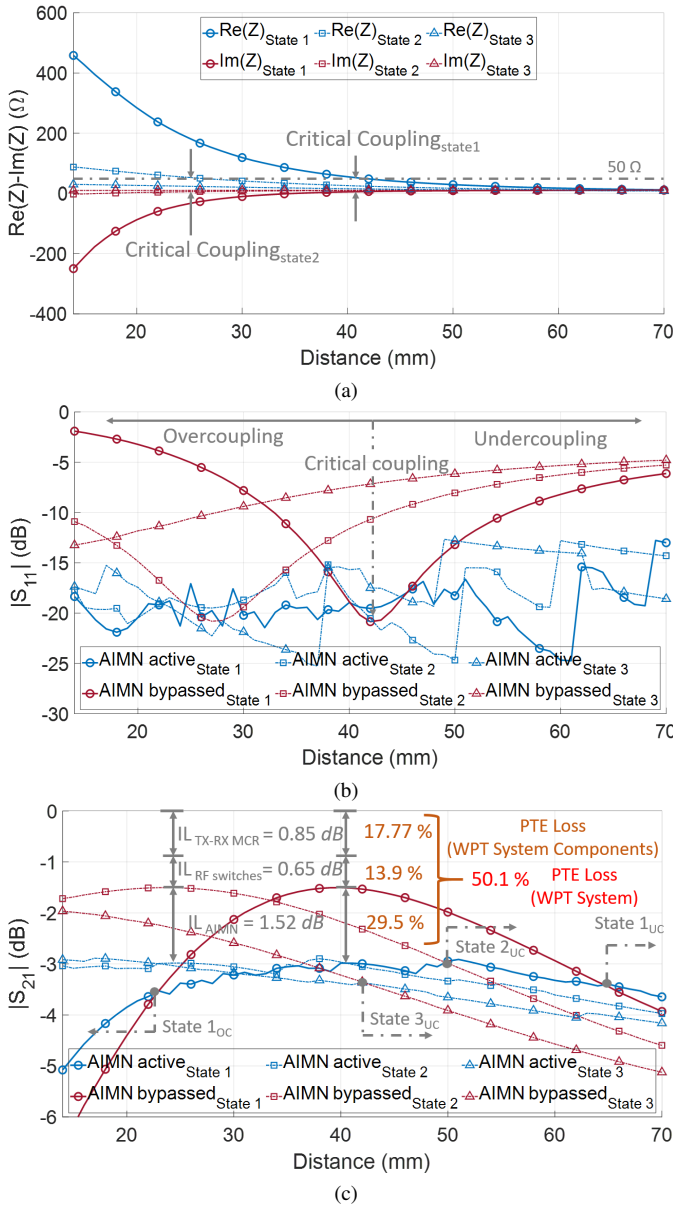


Fig. 7. Performance of the adaptive WPT system over  $d$  with and without the AIMN for three different TX-RX positions: (a) real and imaginary part of  $Z_{in}$ , (b) AIMN reflection coefficient magnitude  $|S_{11}|$  (dB), (c) transmission coefficient magnitude  $|S_{21}|$  (dB). Port 1 and 2 are shown in Fig. 6. The PTE losses (%) of the entire WPT and its components individually are shown in (c). These are calculated as: system  $(1 - |S_{21}|^2)$ , components  $(1 - |10^{-IL/20}|^2)$ .

from Fig. 7b. However, Fig. 7c shows that the increase in matching comes in some cases with a decrease in transmitted power due to the AIMN losses. In these cases, the implemented bypass functionality can be used. Nevertheless, some regions exist at distances far enough from the point of critical coupling for which the AIMN does introduce an enhancement in  $|S_{21}|$  dB, too. These distances are indicated by dashed grey arrows in Fig. 7c for each state (state  $i_{UC/OC}$ ;  $i = 1, 2, 3$ ), and correspond to  $\approx 20$  mm from the point of critical coupling. Particularly, for weakly coupled systems, as in state 3, the AIMN improves  $|S_{21}|$  dB of the system for a significant range of distances, as indicated by state  $3_{UC}$ .

#### IV. CONCLUSIONS

In this work, we have presented and analyzed the performance of an adaptive WPT system implementing an ANN to control an AIMN at the WPT TX which optimizes the system's performance under different relative TX-RX positions. Compared to previous work, we used class 1 ISO/IEC 14443-1 standard coil in the MCRs to investigate the performance of an NFC WPT system. The presented system performance shows that the AIMN controlled by the trained and validated ANN works well. However, the losses introduced by the AIMN overcome the matching gain in some situations, leading to the need to bypass the network. Thus, we presented for the first time a bypass functionality. Future work will include realizing an ANN trained and deciding whether to use the bypass. In addition, we will optimize the AIMN to present lower losses. One potential solution is fully integrating the network into a microchip, reducing the AIMN losses, cost, and carbon footprint. Finally, we will focus on the full hardware implementation of the WPT system, achieving a real-time response.

#### ACKNOWLEDGMENT

This work has been supported by the "University SAL Labs" initiative of Silicon Austria Labs (SAL) and its Austrian partner universities for applied fundamental research for electronic based systems.

#### REFERENCES

- [1] A. Kurs *et al.*, "Wireless Power Transfer via Strongly Coupled Magnetic Resonances," *Science*, 2007.
- [2] T. Ikeda *et al.*, "Application of Wireless Power Transfer to Wearable IoT Devices," in *2022 WPW*, 2022.
- [3] Phantronics. (2022) PTX100W. [Online]. Available: <https://www.phantronics.com/ptx100w/?tab=documentation>
- [4] J. Grosinger *et al.*, "Tag Size Matters: Miniaturized RFID Tags to Connect Smart Objects to the Internet," *IEEE Microw. Mag.*, 2018.
- [5] T. C. Beh *et al.*, "Automated Impedance Matching System for Robust Wireless Power Transfer via Magnetic Resonance Coupling," *IEEE Trans. Ind. Electron.*, 2013.
- [6] G. Lee *et al.*, "A Reconfigurable Resonant Coil for Range Adaptation Wireless Power Transfer," *IEEE T-MTT*, 2016.
- [7] S. Jeong *et al.*, "A Real-Time Range-Adaptive Impedance Matching Utilizing a Machine Learning Strategy Based on Neural Networks for Wireless Power Transfer Systems," *IEEE T-MTT*, 2019.
- [8] Y. Li *et al.*, "An Automatic Impedance Matching Method Based on the Feedforward-Backpropagation Neural Network for a WPT System," *IEEE Trans. Ind. Electron.*, 2019.
- [9] A. P. Sample *et al.*, "Enabling Seamless Wireless Power Delivery in Dynamic Environments," *Proceedings of the IEEE*, 2013.
- [10] Chwei-Sen Wang and Covic, G.A., "Power transfer capability and bifurcation phenomena of loosely coupled inductive power transfer systems," *IEEE Trans. Ind. Electron.*, 2004.
- [11] R. Fischbacher *et al.*, "Broadband EC Models of Coil Antennas for Inductively Coupled Systems," in *2022 IEEE WPW*, 2022.
- [12] M. Gebhart *et al.*, "Design of 13.56 MHz Smartcard Stickers with Ferrite for Payment and Authentication," in *3rd Intl. Workshop on NFC*, 2011.
- [13] M. Wagih *et al.*, "Microwave-Enabled Wearables: Underpinning Technologies, Integration Platforms, and Next-Generation Roadmap," *IEEE J. of Microwaves*, 2023.
- [14] L. Chen *et al.*, "An Optimizable Circuit Structure for High-Efficiency Wireless Power Transfer," *IEEE Trans. Ind. Electron.*, 2013.
- [15] A. P. Sample *et al.*, "Analysis, Experimental Results, and Range Adaptation of Magnetically Coupled Resonators for Wireless Power Transfer," *IEEE Trans. Ind. Electron.*, 2011.